Journal Pre-proofs

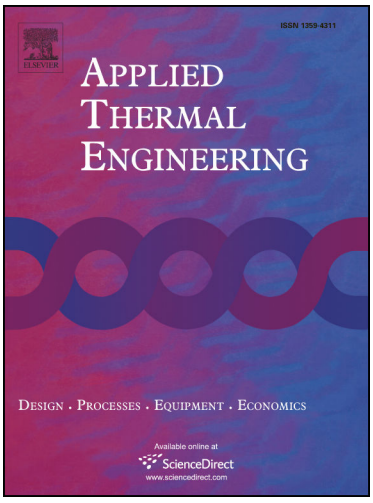

Evaluating the potential of phase-change induced volumetric expansion in thermal energy storage media for passive solar tracking in high-temperature solar energy systems

Barbara Mendecka, Giovanni Di Ilio, Vesselin K. Krastev, Gino Bella

PII: S1359-4311(22)00511-7
DOI: https://doi.org/10.1016/j.applthermaleng.2022.118561
Reference: ATE 118561

To appear in: *Applied Thermal Engineering*

Received Date: 7 December 2021
Revised Date: 11 March 2022
Accepted Date: 20 April 2022

Please cite this article as: B. Mendecka, G. Di Ilio, V.K. Krastev, G. Bella, Evaluating the potential of phase-change induced volumetric expansion in thermal energy storage media for passive solar tracking in high-temperature solar energy systems, *Applied Thermal Engineering* (2022), doi: https://doi.org/10.1016/j.applthermaleng.2022.118561

Evaluating the potential of phase-change induced volumetric expansion in thermal energy storage media for passive solar tracking in high-temperature solar energy systems

Barbara Mendecka[1]*, Giovanni Di Ilio[2], Vesselin K. Krastev[3], Gino Bella[1]

[1] University of Rome "Niccolò Cusano", Rome, Italy
[2] University of Naples "Parthenope", Naples, Italy
[3] University of Rome "Tor Vergata", Rome, Italy

ABSTRACT

As traditional fossil energy sources are continuously diminishing, the demand for optimising output from renewable energy sources is gaining particular importance. Among these, solar energy is certainly one of the most prominent technology and it is widely used in a variety of applications, either concerning electricity and heat production. Nonetheless, the global efficiency of solar systems still has to be largely improved, reducing at the same time generation costs, in order to make solar an even more relevant source of clean energy. In modern photovoltaic, concentrated photovoltaic as well as concentrated solar power plants, the net output can be increased through solar tracking solutions aiming at the optimal positioning of the solar panels/mirrors on a daily and seasonal basis. This typically requires electromechanical motors, which are designed to align the incident solar radiation with the optical axis, thus enhancing the overall energy conversion efficiency but draining at the same time up to 1-2% of the theoretically achievable net power output. Furthermore, to increase energy dispatchability concentrated solar power plants usually incorporates thermal energy storage units, which can be of the sensible-heat or latent-heat storage type. The latter imply phase transition of the storage material which, in turn, can generate up to 20% volumetric expansion for a solid-to-liquid transition. Although generally assumed as an undesired side effect, such expansion can represent an opportunity to extract mechanical work and thus increase the overall efficiency of the solar system. The main objective of this study is to provide an initial quantitative assessment of the passive tracking potential related to the phase-change induced expansion of thermal storage media in concentrated solar power plants. To this aim, a solar-integrated waste-to-heat steam power plant, rated at 15 MWe, has been taken as a reference and a coupled finite-difference/finite-volume numerical model of the latent-heat thermal energy storage unit of the plant has been developed. The model takes input data from the power plant operating conditions and is able to retrieve time-resolved temperature and volumetric density changes of the thermal storage media. Results from the numerical model shows that passive solar tracking is achievable for a fraction of the heliostat field that ranges from 10% to 100%, depending on the season and operating pressure of the tracking system. In terms of electrical power savings, this is up to 2% of the net power output of the reference plant, thus representing a promising basis for further investigations on the applicability of the proposed novel integrated passive solar tracking concept.

Keywords

Phase Change Materials, High-Temperature Thermal Energy Storage, Concentrated Solar Power, Solar Energy, Passive Solar Tracking

* Corresponding author: barbara.mendecka@unicusano.it

Nomenclature

Symbols	
$c_{p,HTF}$	Specific heat capacity of HTF
c_{p_l}	Specific heat capacity of PCM is liquid-phase
c_{p_s}	Specific heat capacity of PCM in solid-phase
ΔH_{latent}	Latent heat of fusion
h_{HTF}	Convective heat transfer coefficient of HTF
H	Specific enthalpy
H_{PCM}	Specific enthalpy of PCM
k_{HTF}	Thermal conductivity of HTF
k_{PCM}	Thermal conductivity of PCM
$\dot{m}_{HTF}$	HTF mass flow
$\dot{m}_{HTF,charging}$	HTF mass flow during charging
$\dot{m}_{HTF,design}$	HTF mass flow at design condition
$\dot{m}_{HTF,dicharging}$	HTF mass flow during discharging
M_{PCM}	Mass of PCM storage
Nu	Nusselt number
r_o	Inner radius of the storage base module
t	Time
T	Temperature
T_{HTF}	Temperature of HTF
$T_{HTF,in}$	HTF inlet temperature
$T_{HTF,out}$	HTF outlet temperature
$T_{l,hot}$	Liquid reference temperature
T_{m_l}	Upper melting temperature
T_{m_s}	Lower melting temperature
T_{PCM}	Temperature of PCM
$T_{s,cold}$	Solid reference temperature
$T_{SH,in}$	Inlet temperature at superheater
$T_{SH,out}$	Outlet temperature at superheater
$\dot{Q}_{max}$	Superheater capacity
$\dot{Q}_{SH}$	Thermal power requested by the superheater
$\dot{Q}_{SR}$	Thermal power produced by the solar receiver
$\dot{Q}_{storage,in}$	Available thermal power for storage
$\dot{Q}_{storage,out}$	Thermal power supplied by the storage
Q_{TES}	Storage capacity
V_{PCM}	Volume of PCM storage
z	Coordinate in axial direction
Greek symbols	
ρ_{HTF}	Density of HTF
ρ_{PCM}	Density of PCM
ρ_s	Density of PCM in solid-phase

1. Introduction

In 2020, the worldwide installed power capacity from renewable energy sources grew more than 260 GW, which is the highest increase ever recorded and beats the previous record of about 200 GW marked in 2019 [1,2]. Nearly half of the new installed capacity in 2020 (about 48%) is covered by solar energy plants, whereas the solar-related annual growth rate has doubled the total renewables-related growth rate (21% vs. 10%). All such data highlights that at present solar energy is the dominant and fastest growing renewable source technology and, therefore, is a key driver for the

achievement of the ambitious mid-term decarbonization and climate change mitigation goals, both in EU as well as at a global level.

The vast majority of solar energy installations is represented by photovoltaics (PV), while a much smaller share is covered by concentrating solar power (CSP) plants. In spite of its minor capacity contribution (about 6.5 GW operational as of 2020, equivalent to 1% of the total installed solar capacity [2]), there is an increasing interest in the CSP technology, especially in some emerging markets located in the global sunbelt region such as the Middle East and North Africa (MENA) area, South America and China [2]. What mainly differentiates CSP from PV is the ability to provide relatively dispatchable electricity, thus improving grid flexibility and reducing the need for fossil fuel backups in low solar irradiance scenarios [1,3]. This is achieved by integrating a thermal energy storage (TES) into the CSP power plant, which allows to introduce up to one day shift between power generation and supply [3]. At the end of 2019, the worldwide CSP-related TES installed capacity was of 21 GWh, while nearly all of the currently operating and already planned or under construction CSP installations incorporate TES concepts [1].

About 95% of global TES capacity in operation on CSP plants is based on sensible heat molten salt technology, with the two-tank direct/indirect arrangement being the most common technical solution [1,3]. The advantages of using molten salt technology are [3]: a relatively high energy density (up to 200 kWh/m^3); an operating temperature of up to 560 °C; a good stability through thermal cycling (more than 10000 cycles) and a lifetime span of more than 20 years. On the other hand, exceeding 560 °C is discouraged, due to the molten salts decomposition tendency above that threshold and the increasing impact of high temperature corrosion on initial and maintenance costs. Furthermore, the two-tank configuration is generally considered more complex and expensive, compared to a single-tank TES [4]. Apart from molten salts, there are only other two TES options for CSP which can be considered commercial-grade: steam accumulators [1,3] and concrete-based solid state sensible heat TES. Steam accumulators have high energy densities and rely on dependable and well proven technologies, but their operating temperature is relatively low and there are severe limits in the scalability potential due to the very high operating pressure. Concrete is competitive with molten salts for operating temperatures up to 500 °C, thanks to its design and deployment simplicity, but the lifetime is currently an issue due to spalling at high temperature and the cracks after repeated thermal expansion/contraction cycles.

Out of the above-mentioned technologies, there are currently several TES alternatives for CSP with various development levels, including: liquid metals, nanofluids, packed bed, particulate solids, thermochemical storage, and latent heat TES (LHTES) [3]. The LHTES principle is based on the adoption of a Phase Change Material (PCM), to accumulate/release large amounts of thermal energy at (nearly) constant temperature. From the requirements imposed upon PCMs it is seen, that they, first of all, should have suitable melting temperature and, whenever possible, high heat of fusion [5,6]. Inorganic salt PCM compounds, such as carbonates, fluorides, and chlorides, can operate at temperatures above 400 °C, which makes them suitable for CSP storage applications [7-9]. Advantages of LHTES consist of very high energy densities (smaller tank volumes) and lower deployment complexity compared to other storage media. On the other hand, a number of drawbacks hinders their actual implementation at commercial scale levels, namely [10,11]: incongruent melting, subcooling temperature shifts, highly corrosive nature and slow charge/discharge rates. Moreover, the narrow inlet/outlet temperature range can often introduce additional system integration difficulties. An additional secondary effect during LHTES operation is the significant volumetric expansion occurring at the solid-to-liquid phase transition, which may range from a few percentage points up to 20% or more [12]. Such expansion is commonly assumed as a technical constraint, which has to be taken into account in the thermo-mechanical design of the LHTES system [12,13], but with no actual role in the energy charge and discharge processes. Conversely, the same expansion effect has a key role in other engineering applications: some widespread low-temperature PCMs, such as paraffin waxes, have been used as actuation media for many years, thanks to the large amount of mechanical work expressed by their thermally driven expansion [14-17]. More recently, the driving force

potential of PCMs has been considered for the realization of thermally driven fully passive solar trackers [18,19]. In such devices, a relatively small amount of PCM is melted by solar radiation, generating a torque output that is solely used for single axis tracking in standard PV panels.
All the currently operational CSP plant configurations: parabolic trough collectors (PTC), solar power tower (SPT), linear Fresnel reflector (LFR) and parabolic dish systems (PDS), require solar tracking to continuously adjust the optimal orientation of mirrors/heliostats with respect to the sun and concentrate solar radiation onto the fixed absorber/receiver [20]. The PTC and LFR configurations achieve that with single-axis tracking, while in SPT, a complex two-axis tracking algorithms and feedback sensors are needed to simultaneously monitor and correct the orientation of a large number of heliostats [21]. As opposed to conventional power generation systems, for CSP initial investment represents about 80% of the cost of the generated electricity, while the remaining 20% originates from the plant's operational and maintenance costs, which in turn are largely related to the tracking system [21,22]. From an energy balance point of view, tracking introduces also net conversion efficiency losses, due to the power consumption of electrical motors and drives [23-25].
In a previous work of the authors, the feasibility of using the volumetric expansion cycles in a PCM-based TES device for PV solar tracking purposes has been assessed [26]. The scope of the present study is to evaluate a high temperature LHTES (HT-LHTES) solution for CSP, which integrates solar tracking capabilities thanks to the spontaneous volumetric expansion induced in the PCM storage media during thermal cycles. The underlying principle is to possibly rely on a standard LHTES technical infrastructure, avoiding the need for active energy inputs to control tracking over time. Specifically, the study is carried out for a PCM-based TES integrated into a Waste to Energy (WtE) steam power plant coupled with SPT. A 2D finite-difference/finite-volume numerical model is developed and used to evaluate the transient temperature field inside the PCM medium and its related volumetric expansion, under realistic operating scenarios provided by the data available from the reference power plant. Thus, the tracking potential for the heliostats of the system is estimated and provided in a parametric way by assuming a range of working actuation pressures. To the best of the authors' knowledge and based on the above cited literature references, this is the first time a similar passive efficiency-enhancing solution is proposed for high-temperature solar plants.

2. Materials and methods

The design and operation of the HT-LHTES considered in this study have been performed basing on data from a previously investigated solar hybrid WtE Rankine cycle [23-25]. The specific case study of a solar integrated WtE plant with a thermal power input of 50 MW and operating with externally superheated steam at 60 bar and 480 °C, without re-heating, is selected in this work. The heliostat field, which is dimensioned based on the mass flow rate of saturated steam produced in the WtE section, consists of 710 units, each having an overall surface of 120 m^2. Detailed assumptions and design parameters for the receiver and simulation of the Rankine cycle can be found in previous work by authors [24]. Figure 1 reports a schematic layout of the considered power plant.

In the considered system, the WtE plant boiler is designed to produce only saturated steam at the design pressure, by means of economizer and evaporator. Saturated steam, before heading to the steam turbine, is then superheated in an external heat exchanger (SH in Figure 1). Heat flux to SH can be supplied by either the SPT or the gas boiler, which can be combined or used independently, depending on the current operating conditions.
Superheated steam feeds the high-pressure steam turbine, and then through medium-pressure and low-pressure sections reaches the air-cooled condenser. Condensate from the condenser is supplied to the boiler through a one-stage regenerative heat exchanger and deaerator. Usable products of the cycle comprise only electricity (net power output).

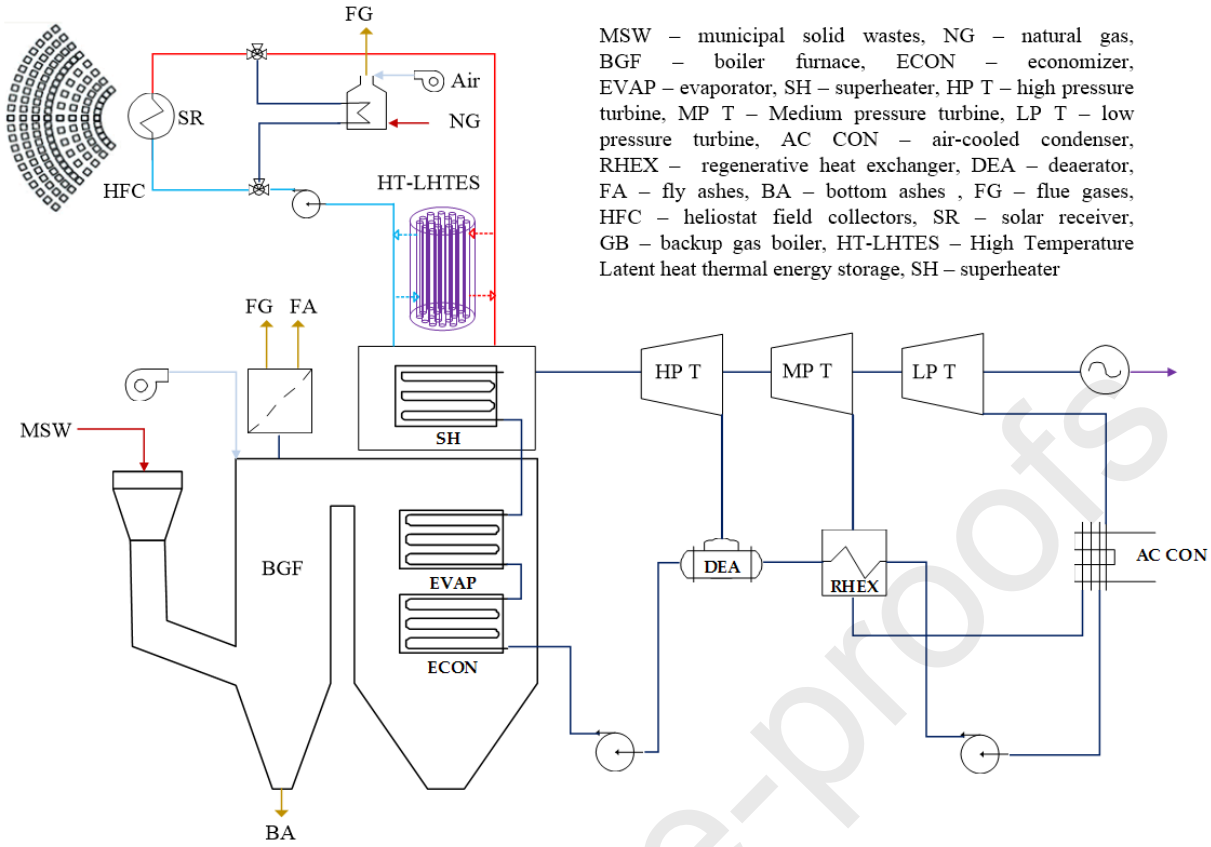

Figure 1 – Schematic representation of the considered WtE–SPT power plant.

The integrated SPT makes use of a heliostat field collector (HFC), i.e., a field of sun-tracking reflectors, that reflect and concentrate the sun rays onto a central solar receiver (SR) placed on the top of a fixed tower. In the SPT cycle, molten salts mixture ($60NaNO_3$–$40KNO_3$) is considered as the heat transfer fluid (HTF). The thermal power output of SR and the HTF mass flow rate vary with time, however the SR outlet temperature is fixed at 565 °C, since the selected HTF is characterized by a usable temperature range of 290-565 °C [27]. The pinch point temperature difference in the evaporator is set at 25 °C.

Molten salts are pumped through the SR, where they are heated; they then supply the superheater at its rated design capacity. The exceeding thermal energy is stored in a shell and tube HT-LHTES (differently from [23-25] where an indirect two-tank molten salts system was considered). In the proposed configuration, the HTF and the PCM medium are separated by the walls of the piping and PCM is located in the shell. During discharging, cold salts at 301 °C coming from the superheater are pumped into the TES, where they heat up, so that they can recirculate and feed the superheater.

A simple control system is considered for the CSP section energy management. The control objective is to supply superheated steam at the demanded temperature and pressure, minimizing auxiliary energy (gas) consumption. This assumes that the gas boiler operates only when the HT-LHTES is discharged below a pre-defined threshold (i.e. the exiting HTF is at 450 °C), and there is no (or not enough) solar power from the SR available. Additionally, when the HT-LHTES capacity is saturated, the control does not allow its charging above the maximal capacity. In the situation when HT-LHTES is fully charged and superheating requirements are covered, the exceeding part of solar energy available at the SR is dumped, e.g., by means of heliostat defocusing.

For the design of the CSP section of the plant, a hypothetical site in south of Italy (13.1 °E ; 38.2 °N) is selected as a representative case of high solar irradiance. Solar Multiple (SM) parameter which represents the solar field size related to the power block requirements is assumed to be equal to 2. All the key parameters for the CSP section design are shown in Table 1.

Table 1 – Design point parameters for the solar field.

Parameter	Value
Direct Normal Irradiance [W/m^2]	600
Design Solar Multiple [-]	2
Superheater capacity [MW]	10.5
Area of heliostats [m^2]	85200
Number of heliostats	710
Average temperature [°C]	18.8
Average wind speed [m/s]	3.8
Longitude	38.2 °N
Latitude	13.1 °E

A binary eutectic mixture of molten lithium carbonates ($35Li_2CO_3$–$65K_2CO_3$) is chosen as storage material [28-30], given its high melting temperature which is consistent with the requirements of the considered application. Moreover, such a material is characterized by a relatively high thermal energy storage capacity and volumetric expansion. Table 2 summarizes the main thermo-physical properties of the selected PCM and HTF.

Table 2 – PCM and HTF thermo-physical properties.

Properties	Unit	PCM $35Li_2CO_3$–$65K_2CO_3$ [28-30]	HTF $60NaNO_3$–$40KNO_3$ [31-32]
Dynamic viscosity	[kg/m s]	-	0.0022
Solid density	[kg/m^3]	2260	-
Liquid density	[kg/m^3]	2010	1815
Solid specific heat capacity	[J/kg K]	1340	-
Liquid specific heat capacity	[J/kg K]	1760	1518
Solid thermal conductivity	[W/m K]	2.25	-
Liquid thermal conductivity	[W/m K]	1.89	0.5253
Latent heat of fusion	[kJ/kg]	344	-
Lower melting point	[°C]	502	-
Upper melting point	[°C]	508	-

In order to determine the HT-LHTES size, a storage capacity (Q_{TES}) of 12 h with the superheater operating at full load has been assumed, that is about 126.1 MWh (453.9 GJ). Also, the heat storage capacity of PCM is considered as the sum of both sensible and latent heat contributions, between the reference temperatures $T_{s,cold} = 490$ °C and $T_{l,hot} = 520$ °C. Therefore, the PCM storage mass and volume are calculated as follows [33,34]:

$$M_{PCM} = \frac{Q_{TES}}{c_{p_s}(T_{m_s} - T_{s,cold}) + \Delta H_{latent} + c_{p_l}(T_{l,hot} - T_{m_l})} \quad (1)$$

$$V_{PCM} = \frac{M_{PCM}}{\rho_s} \quad (2)$$

where T_m is the melting temperature of PCM, c_p and ρ are its specific heat capacity and density, respectively, while ΔH_{latent} is the latent heat of fusion. Subscripts *s* and *l* in equations (1) and (2) indicate *solid* and *liquid*, respectively. The resulting mass and volume of PCM to fill the TES are equal to 1191 t and 527 m^3, respectively.

Further, in line with typical HT-LHTES systems for solar thermal power plants, and basing on the

HTF mass flow rate from SR at design conditions, we assume the storage tank to be 10 m high and ideally composed of 3494 base modules, each being constituted by a concentric cylindrical structure: the HTF flows through the inner tube, while the outer cylinder is filled by PCM. The inner and outer radius of each base module are taken equal to 0.04 and 0.08 m, respectively, while the thickness of the tubes is considered negligible.

2.1 Numerical modelling of the HT-LHTES system

Several mathematical and numerical approaches have been suggested in literature to model PCM systems. These encompass simplified methodologies based on correlation functions as well as complex computational models to predict the transient behaviour of the PCM [35-36]. The approach chosen in this work has the key advantage of retaining all the relevant physics needed to properly characterize the thermal behaviour of a generic PCM, while neglecting minor effects which are not essential in the context of an energy system analysis as the one proposed in this study. In particular, the mathematical background behind the adopted numerical modelling is based on the following assumptions [34,37,38]:

1. the PCM medium is homogeneous and isotropic;
2. the thermal resistance of the HTF tubes is negligible;
3. the PCM properties are temperature-independent, although they depend on phase. In particular, thermal conductivity and density varies linearly during the phase transition;
4. the natural convection in the PCM during phase transition and in liquid phase is not considered;
5. the HTF flow is assumed to be 1D;
6. the axial conduction in the HTF is negligible;
7. the storage tank is thermally insulated, thus no heat losses are considered.

Basing on these assumptions, the mathematical model for the transient thermal behaviour of the HT-LHTES can be described by the following two coupled heat transfer equations, for HTF and PCM, respectively:

$$\rho_{HTF} c_{p,HTF} \pi r_o^2 \frac{\partial T_{HTF}}{\partial t} = - \dot{m}_{HTF} c_{p,HTF} \frac{\partial T_{HTF}}{\partial z} + h_{HTF} (T_{PCM|r=r_o} - T_{HTF}) 2\pi r_o \quad (3)$$

$$\rho_{PCM} \frac{\partial H_{PCM}}{\partial t} = \nabla \cdot (k_{PCM} \nabla T_{PCM}) \quad (4)$$

where r_0 is the inner radius of each base module, $\dot{m}_{HTF}$ is the HTF mass flowing in each tube, h is the convective heat transfer coefficient, H is the specific enthalpy and k is the thermal conductivity. In particular, the HTF convective heat transfer coefficient is computed as follows:

$$h_{HTF} = \frac{Nu \cdot k_{HTF}}{2\mathrm{r_o}} \quad (5)$$

where Nu is the Nusselt number, which is equal to 3.66, since the HTF flow is laminar.
As far as the computation of the PCM enthalpy, this is evaluated by a simple and widely used approach, according to which the enthalpy is a function of the temperature, as follows:

$$H = \begin{cases} c_{p,s}T & \text{for } T < T_{m_s} \\ c_{p,l}T + \dfrac{\Delta H_{latent}(T - T_{m_s})}{T_{m_l} - T_{m_s}} & \text{for } T_{m_s} < T < T_{m_l} \\ c_{p,l}T + \Delta H_{latent} & \text{for } T > T_{m_l} \end{cases} \quad (6)$$

Equations (3)-(4) are numerically solved on a 2D axisymmetric computational domain, for a single HT-LHTES module, by means of a coupled approach based on an implicit finite-difference/finite-volume method [39,40]. Further details on the implementation of this method can be also found in [26] where the authors have already used it and validated it for analysing the PCM thermal behaviour in a LHTES integrated in a photovoltaic solar-assisted heating/cooling plant.

As far as the numerical setup, we set adiabatic walls for the external module surfaces, while the heat transfer between PCM and HTF is ensured by setting the conductive heat flux from PCM equal to the convective one from the HTF. A fixed inlet temperature, at each time-step, according to the specific load profile, is set for the HTF flow, while a zero thermal flux condition is imposed at its outlet. In particular, depending on the HT-LHTES operation (charging/discharging mode), the HTF flows in a direction or in its opposite, in such a way to keep a hotter side and a colder side, during the whole power plant operation. This strategy allows to improve the thermal efficiency of the storage system.

A structured non-uniform fixed mesh is employed for all simulations of this work, which suitable resolution has been already assessed in [26]. This consists of 101 × 11 elements, leading to a spacing of 0.004 m and 0.1 m in the radial and axial directions, respectively. Time resolution is chosen according to input data availability, that is 60 s. In all simulations, the whole computational domain is initialized with uniform temperature, which value is chosen depending on the specific case under consideration, as will be detailed later.

2.2 Evaluation of heliostat tracking capacity

In this study, it is assumed that the heliostat field is composed of two-axis tracking mirrors. In particular, the rotation of the optical axis of the heliostat is performed by means of dual-axis azimuth-elevation tracker, in such a way to keep the heliostat surface in an optimal position to the solar radiation during all daylight hours. Also, the position angles are adjusted considering not only the sun position but the target position of the SR as well. Each heliostat is therefore driven by a pair of motors, one for each tracking axis, which are supplied from a DC line. Specifically, the heliostat mirror considered in this work is the commercially available Sener HE35 [41].

Table 3 – Heliostat specifications and assumed design parameters.

Parameter	**Value**
Heliostat mirror area/total area [m^2]	115.7/120
Heliostat length [m]	9.75
Heliostat height [m]	12.30
Heliostat diagonal [m]	15.70
Drag coefficient, [-] (flat surface)	1.4
Wind velocity, [m/s]	10

Its technical specifications along with other assumptions used to estimate both the mechanical actuation energy required to provide full day heliostat tracking capacity and the servomotors design calculations for the conventional solar tracking system are presented in Table 3.

The required torque needed for the tracking of the heliostat mirror considers that the most significant force acting on the surface of the heliostat is the aerodynamic force from wind. This can be estimated by assuming a reference wind speed condition, as per Table 3. Thus, by considering the maximum daytime rotations about the two axis, we estimate that an actuation energy of about 170 kJ is required to provide a full-day dual axis tracking course of a single heliostat.

The proposed actuation concept assumes that the expansion of the PCM medium is exploited by means of a mechanical device, such a hydraulic actuator, which ultimately provides the dual axis motion to rotate heliostats. Therefore, in order to evaluate the actual tracking capacity, that is the volumetric expansion required to ensure actuation energy for the tracking motion of 1 m^2 of installed heliostat, a working actuation pressure must be assumed. Since a detailed analysis of the actuation mechanisms is not yet available at this stage of research, we arbitrarily consider a working pressure ranging between 5 and 50 bars, in order to provide results in a parametric way. Table 4 collects the outcomes from this analysis.

Table 4 - Heliostat tracking capacity estimation.

Parameter	Value
Actuation energy [kJ/heliostat]	170
Actuation energy [kJ/m^2]	1.4
Working pressure [bar]	5 – 50
Tracking capacity [m^2/L]	0.35 – 3.53

To estimate the potential benefit given by the proposed solution, in terms of net electric power output gain, the power consumption of electrical motors for conventional tracking has been evaluated. By considering design operating conditions, and an overall efficiency of 0.8 for the tracking system, a value of around 0.30 kW of required power is calculated for each heliostat. This leads to a total amount of roughly 200 kW to feed the whole solar field. According to the analysis presented in [24], the considered solar integrated WtE power plant provides around 14.8 MW of net electricity output. Therefore, the overall power consumption of electrical motors accounts for 1-2 % of the net power output.

3. Results and discussion

The temporal evolution of the PCM temperature and density fields inside the storage tank is computed numerically in order to assess the effective volumetric expansion during typical charging/discharging cycles of the HT-LHTES system. However, before dealing with a real-case scenario, preliminary tests considering single reference charging and discharging processes are simulated, in order to check for modelling assumptions consistency and verify the proposed storage design.

3.1 Charging/discharging process with HTF inflow at constant temperature

For the charging process, the HTF inflow is set at 565 °C, while the temperature field is initialized at 301 °C everywhere in the domain. Conversely, for the discharging process, the HTF enters the storage tank at 301 °C while the initial temperature of the whole system is 565 °C. As already mentioned, these two limit temperatures correspond to those at the SR outlet/superheater inlet and at the superheater outlet, respectively, therefore these are the actual values of the HTF mass flow entering the storage tank during real operating conditions. For both charging and discharging cases, the HTF mass flow is assumed to be constant and it is taken equal to its designed value, that is:

$$\dot{m}_{HTF,design} = \frac{\dot{Q}_{max}}{c_{p,HTF}(T_{SH,in} - T_{SH,out})} \tag{7}$$

where $T_{SH,in} = 565$ °C and $T_{SH,out} = 301$ °C, while $\dot{Q}_{max}$ is the superheater capacity (Table 1). Figure 2 shows the resulting temperature profiles for the simulated charging and discharging processes, while in Figure 3 the obtained volumetric expansion in the two cases is depicted.

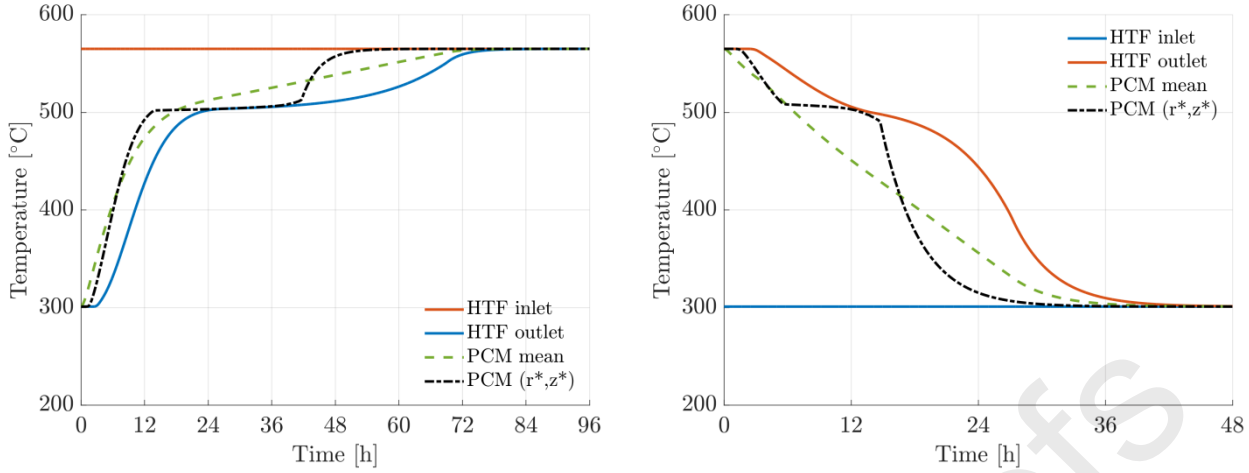

Figure 2 – Temperature profiles in the HT-LHTES for reference charging (left panel) and discharging (right panel) processes. The curves refer to HTF inlet, HTF outlet, PCM mean, and to a probe within the PCM at $r^* = 0.06$ *m and* $z^* = 5$ *m.*

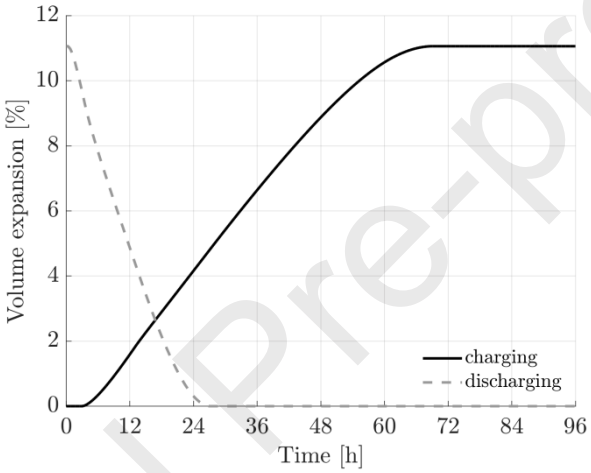

Figure 3 – Volume expansion during reference charging and discharging processes, as a function of time.

The resulting temperature profiles are consistent and, in particular, the phase transition in the PCM medium is well captured by the model. In particular, this gives rise to an increase/decrease of the PCM volume of about 11%, as expected (Table 2). Such an expansion is achieved in roughly 72 and 24 hours for charging and discharging, respectively. Also, from the results, the PCM takes about 78 hours to reach the equilibrium temperature under reference charging conditions, while it takes 42 hours to fully discharge. It should be noted that the different thermal behaviours observed for the two cases can be ascribed to the different temperature ranges between the melting/solidification point and the target temperature (i.e. HTF inlet temperature). In fact, such a temperature range is lower for the charging process, which corresponds to a lower available heat transfer rate for melting. Therefore, the melting rate of PCM during charging is lower than the solidification rate during discharging. This leads to different process times, but also to a different interdependency between expansion and temperature curves, in the two cases. Also, it has to be emphasized that the results on volume expansion reported in Figure 3 are related to the chosen materials. That is, a possibly higher asymptotic value (considering the charging process) would have been obtained by selecting a different storage material, and a higher volume expansion rate could be achieved by using a molten salts mixture of different thermo-physical properties as HTF, among those typically employed for the present application. Beside thermo-physical properties, also the HTF mass flow plays a role in the determination of the charging/discharging times. In this case, the HTF mass flow has been taken as a constant parameter corresponding to the design operative condition, therefore the resulting charging/discharging times should be regarded as reference values.

Next, the temperature and density fields within the PCM medium are shown at different times during both charging (Figure 4-5) and discharging (Figure 6-7) processes. The results in Figure 4-7 are given for an axisymmetric portion of a single reference HT-LHTES module. The temperature distribution within the storage tank and the propagation of the melting/solidification front are accurately described by the numerical model. In particular, the solid-to-liquid interface moves from the pipe surface -in the proximity of the HTF inlet- toward the outer region of the HT-LHTES module, as expected.

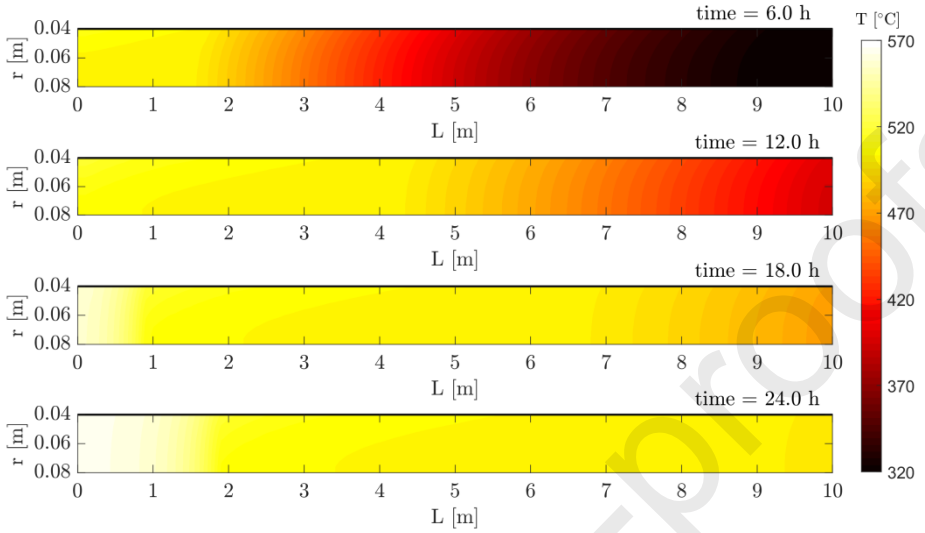

Figure 4 – PCM temperature field at different times during the reference charging process. The HTF flows at the inner radius from the left to the right.

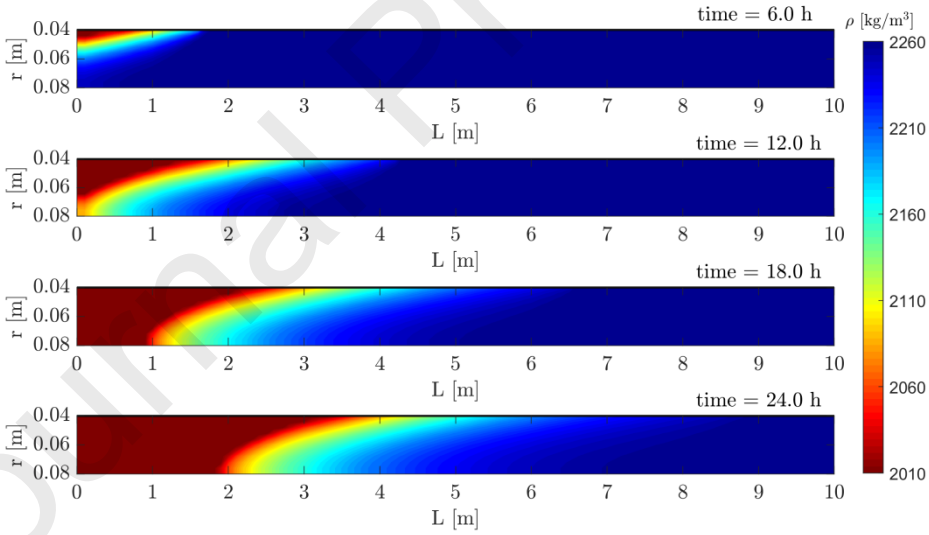

Figure 5 – PCM density field at different times during the reference charging process. The HTF flows at the inner radius from the left to the right.

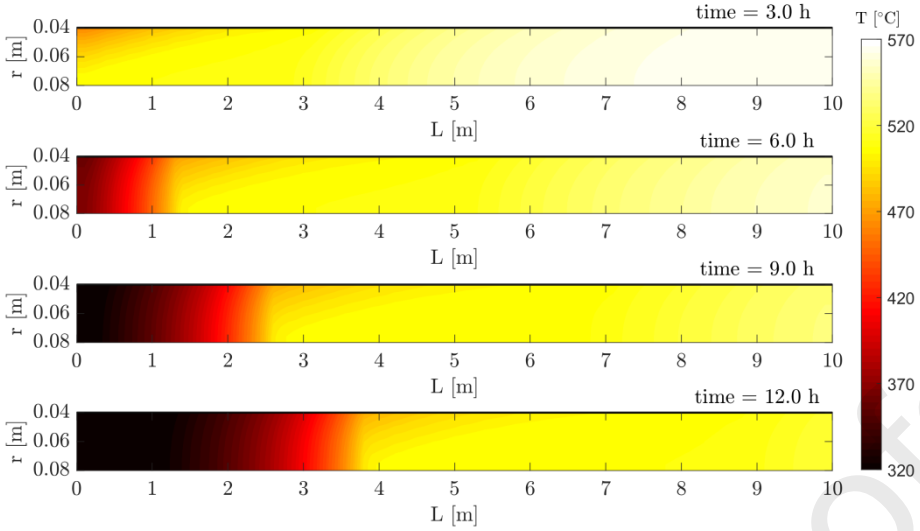

Figure 6 – PCM temperature field at different times during the reference discharging process. The HTF flows from at the inner radius from the left to the right.

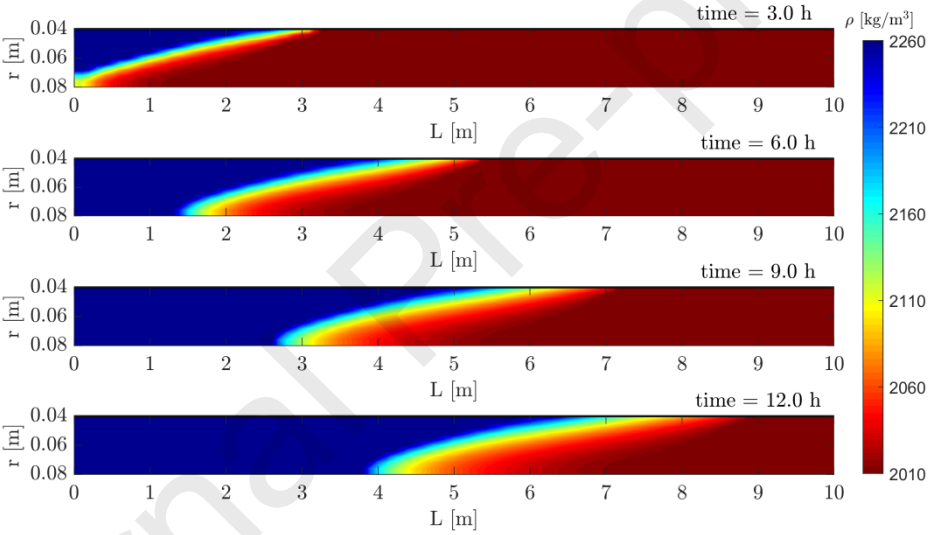

Figure 7 – PCM density field at different times during the reference discharging process. The HTF flows at the inner radius from the left to the right.

Further, the temporal evolution of the cross-section average temperature profile in the PCM is shown in Figure 8, for both charging and discharging processes. The transient thermal behaviour of the PCM is properly retrieved, with the melting/solidification range being suitably characterized by the flattening of the curves, which indicates the presence of isothermal regions within the media, where the phase change is occurring.

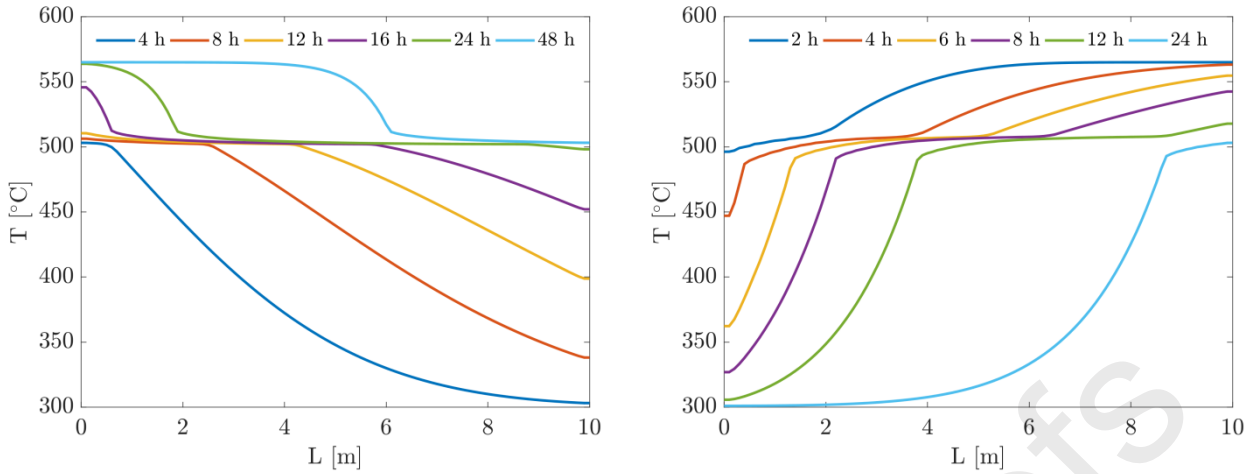

Figure 8 – Time evolution of the average temperature profiles measured at the cross-section of the PCM region. Left: charging process; right: discharging process.

3.2 Real operating conditions

Next, realistic operating conditions are simulated, in order to understand the thermal behaviour of the PCM within the storage tank and to provide a fair estimation of the heliostat tracking potential. Specifically, two periods of the year are considered: the months of January and July, during which the power plant experiences quite dissimilar operating conditions, due to the different solar radiation. In both cases, a time-dependent HTF inlet temperature profile is imposed, corresponding to the off-design performance of the power plant: the HTF inlet temperature is equal to 565 °C during the charging of the storage tank (i.e. when the SR produces an exceeding amount of thermal power) or 301 °C during discharging (i.e. the thermal power from SR is not sufficient to cover the SH power demand). Consistently, also the HTF mass flow is a time-dependent function, as follows:

$$\dot{m}_{HTF,charging} = \frac{\dot{Q}_{storage,in}}{c_{p,HTF}(T_{SH,in} - T_{SH,out})} \quad , \quad \dot{Q}_{storage,in} = \dot{Q}_{SR} - \dot{Q}_{SH} > 0 \tag{8}$$

$$\dot{m}_{HTF,dicharging} = \frac{\dot{Q}_{storage,out}}{c_{p,HTF}(T_{HTF,out} - T_{HTF,in})} \quad , \quad \dot{Q}_{storage,out} = \dot{Q}_{SH} - \dot{Q}_{SR} > 0 \tag{9}$$

where $\dot{Q}_{storage,in}$ is the available thermal power for storage occurring when the thermal power produced by the SR ($\dot{Q}_{SR}$) is greater than the requested thermal power of the superheater ($\dot{Q}_{SH}$) and, conversely, $\dot{Q}_{storage,out}$ is the thermal power that has to be supplied to the superheater in order to fulfil its power request whenever this cannot be covered by the SR only. For both the simulated scenarios, the initial temperature field in the HT-LHTES is set equal to 490 °C. Thus, the PCM is assumed to be in solid phase at the beginning of the simulations.

The results from simulations, in terms of temperature profiles, are shown in Figure 9-11. In the figures, the vertical grey bands correspond to the time intervals during which the HT-LHTES is not charged neither can be discharged, that is when the outflow HTF temperature reaches 450 °C.

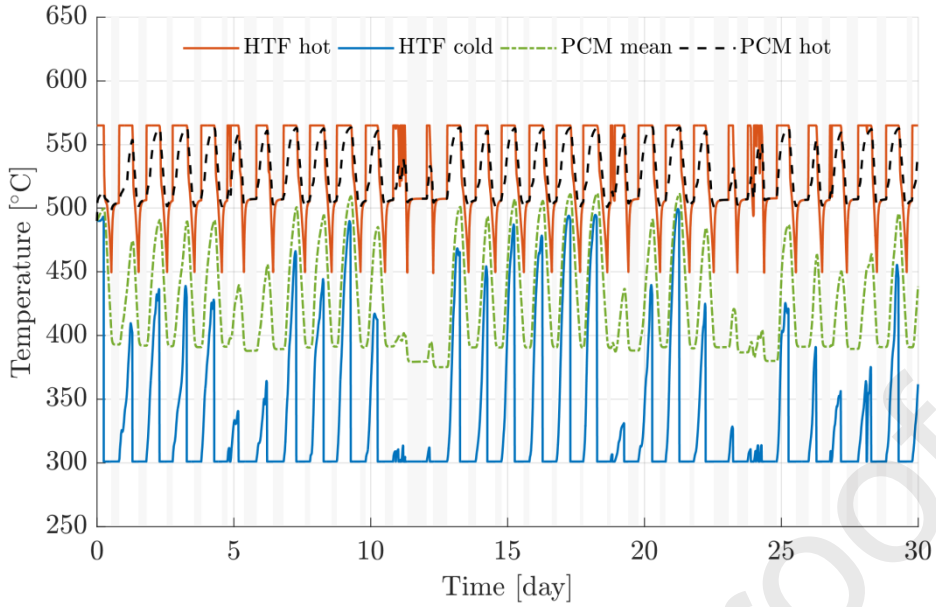

Figure 9 – Temperature profiles in the HT-LHTES during summer. The curves refer to HTF hot and cold sides, PCM mean, and to a point in the PCM located at the closest proximity of the HTF hot side. Vertical grey bands indicate time intervals with no HTF flow within the tank.

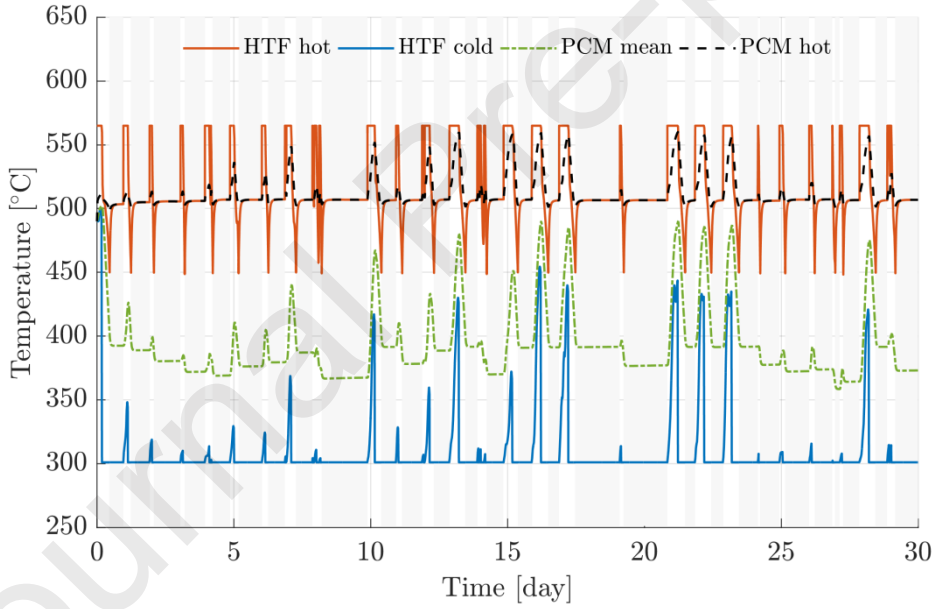

Figure 10 – Temperature profiles in the HT-LHTES during winter. The curves refer to HTF hot and cold sides, PCM mean, and to a point in the PCM located at the closest proximity of the HTF hot side. Vertical grey bands indicate time intervals with no HTF flow within the tank.

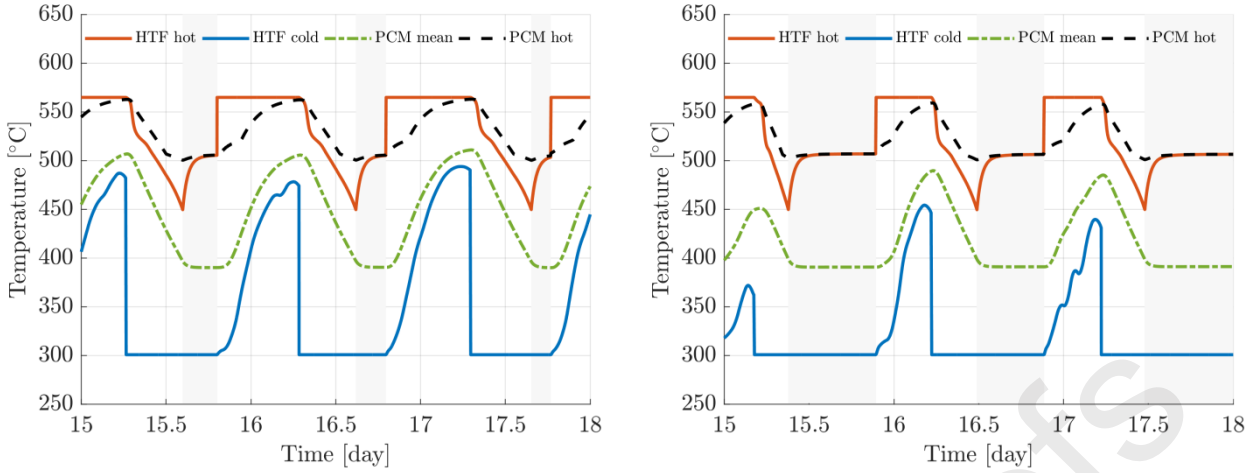

Figure 11 – Detail of temperature profiles in the HT-LHTES during summer (left) and winter (right), for three reference days.

We emphasize that the HTF hot/cold sides reported in Figure 9-11 correspond to either the HTF inlet or outlet depending on the specific operation: the HTF hot side is the HTF inlet during charging and it is the outlet during discharging; vice versa, the HTF cold side corresponds to the inlet during discharging, while it is the HTF outlet when the HT-LHTES is charged. As expected, the PCM mean temperature undergoes a cyclic variation, which follows the HTF input temperature profile. Also, the time-averaged temperature in PCM is significantly higher in summer, during which the HT-LHTES is capable to compensate the thermal power requested by the superheater, for most of the time of power plant operation. In contrast, due to the diminished share of solar radiation in winter, the HT-LHTES operation is less effective during this period of the year. In winter, the lower availability of thermal power from the SR leads indeed to shorter charging times of the storage tank. Figure 12 shows the HTF mass flow profiles, for a reference week during both the analysed periods, which further emphasize these findings.

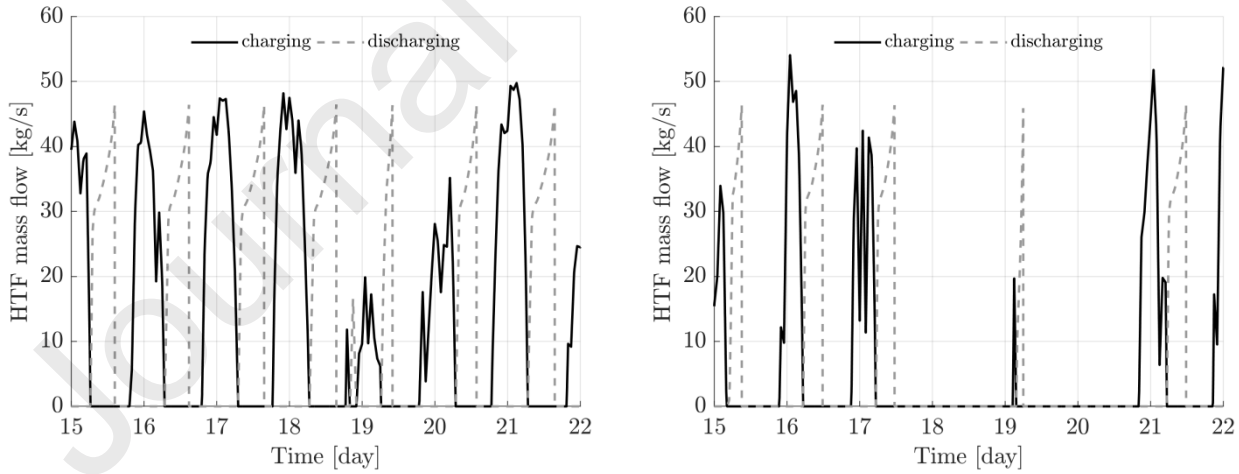

Figure 12 – HTF mass flow profiles during a reference week in summer (left) and winter (right). Blue solid lines refer to the charging process, while black dashed lines correspond to the discharging of the storage tank.

The thermal behaviour of PCM so far described lead to a PCM volume expansion variation in time, which is shown in Figure 13, for both the considered cases.

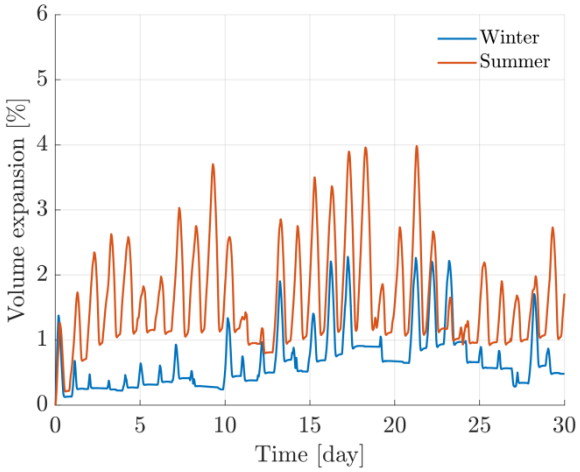

Figure 13 – PCM volume expansion during a reference month in summer and winter.

Clearly, the volume expansion is less pronounced during winter, where the lower availability of solar radiation negatively affects the actual heat storage capacity of the system. On the other hand, the volume expansion of PCM during summer is significant, and its cycle variation appear to be quite regular during the whole period analysed. The maximum achieved volume expansion in winter is around 2%, while during summer this hit a peak of roughly 4%. Although, it should be noted that the PCM volume is about the 1% higher than that related to its solid phase, during the whole summer period. This indicates that the actual useful expansion is reduced by this amount. By taking into consideration this aspect, the mean volume expansion per day computed by our model are 7870 L and 3384 L, in summer and winter, respectively. Basing on these values the actuation potential of PCM, that is its ability of providing the necessary energy to perform the solar tracking of heliostat, is assessed.

Thus, by considering the estimated tracking capacity (Table 4), the mean number/surface of actuated heliostats that can be achieved is evaluated parametrically for a range of working pressure. The results are presented in Figure 14.

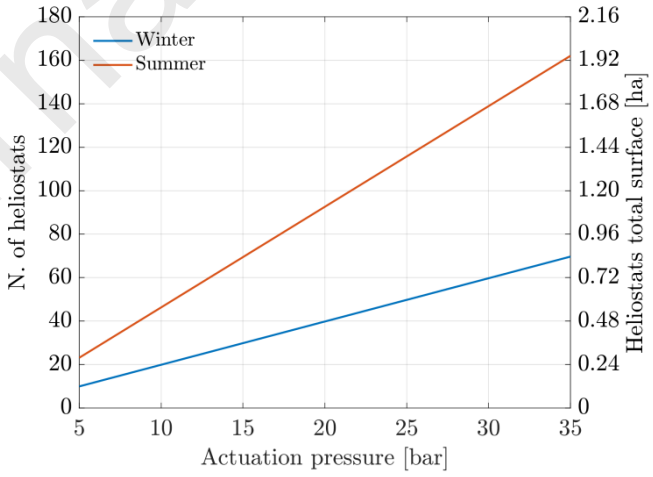

Figure 14 – Tracking capability of the PCM, expressed in terms of mean number of actuated heliostats and mean total surface of the actuated heliostats per day, during two reference months.

The significant amount of PCM volume expansion leads, potentially, to an effective passive solar tracking of the heliostat field. A high number of heliostats, or even the whole field, could be in principle passively controlled by an actuation mechanism operating at relatively low pressure. As an example, by assuming a working pressure of 35 bar, the passive solar tracking can be performed to the 10% of the whole heliostat field during winter, that is the most critical scenario. A working

pressure of roughly 150 bar would be instead theoretically sufficient to perform the solar tracking of the whole heliostat field in summer. Despite these calculations do not take into account the actual design of the mechanical actuator, as well as its specific integration into the HT-LHTES system, they still demonstrate the great potential of the proposed concept to boost solar-based applications.

4. Conclusions

This paper presents an original concept of passive solar tracking for CSP-integrated power systems. The idea is to exploit the significant volume expansion of a PCM within a HT-LHTES, to perform the thermally-driven actuation of the heliostat field. To this aim, realistic operating conditions of a solar hybrid WtE power plant are considered and the thermal behaviour of the PCM contained in the integrated storage tank is studied by means of a detailed numerical model. This considers actual time-dependent charging and discharging temperatures and HTF mass flow profiles, as input for the storage device.

Based on energy arguments, the findings from this study reveal that the passive solar tracking is theoretically feasible for a significant share of the heliostat field for a mid-sized CSP plant (10-20 MWe). More specifically, assuming a moderate working pressure (below 50 bar) a 10-20% passive tracking share is achievable, depending on the season. If the working pressure is raised to at least 150 bar, a 100% passive tracking share is achievable in summer, leading to a potential 2% increase in the net power output. Although further consolidation work is required (e.g. a study on the actual thermo-mechanical design of the integrated TES-tracking system), the presented results open interesting perspectives in the development of multifunctional LHTES devices as a viable solution for increasing efficiency and lowering energy production costs in solar power plants.

Abbreviations

CPV	Concentrated Photovoltaic
CSP	Concentrated Solar Power
HFC	Heliostat Field Collector
HSM	Heat Storage Materials
HTF	Heat Transfer Fluid
HT-LHTES	High Temperature Latent Heat Thermal Energy Storage
LFR	Linear Fresnel Reflector
LHTES	Latent Heat Thermal Energy Storage
PCM	Phase Change Material
PDS	Parabolic Dish System
PTC	Parabolic Trough Collectors
PV	Photovoltaic
SM	Solar Multiple
SPT	Solar Power Tower
SR	Solar Receiver
TES	Thermal Energy Storage
WtE	Waste to Energy

References

[1] United Nations Environment Programme. Renewables 2020 Global Status Report (2020).

[2] International Renewable Energy Agency (IRENA). Renewable capacity statistics 2021.

[3] Palacios A, Barreneche C, Navarro ME, Ding Y, "Thermal energy storage technologies for concentrated solar power – A review from a materials perspective", Renew. Energy 156:1244–65 (2020), doi:10.1016/j.renene.2019.10.127.

[4] Fleischer AS, "Thermal energy storage using phase change materials: Fundamentals and applications" (2015), doi:10.1007/978-3-319-20922-7.

[5] Xu B, Li P, Chan C, Fine JP, Friedman J, Dworkin SB, et al. "Application of phase change materials for thermal energy storage in concentrated solar thermal power plants: A review to recent developments", Appl. Energy 160:286–307 (2015), doi:10.1016/j.apenergy.2015.09.016.

[6] Wei G, Wang G, Xu C, Ju X, Xing L, Du X, et al. "Selection principles and thermophysical properties of high temperature phase change materials for thermal energy storage: A review", Renew. Sustain. Energy Rev. 81:1771–86 (2018), doi:10.1016/j.rser.2017.05.271.

[7] Myers PD, Goswami DY. "Thermal energy storage using chloride salts and their eutectics", Applied Thermal Engineering 109:889–900 (2016), doi:10.1016/j.applthermaleng.2016.07.046.

[8] Li Q, Li C, Du Z, Jiang F, Ding Y, "A review of performance investigation and enhancement of shell and tube thermal energy storage device containing molten salt based phase change materials for medium and high temperature applications", Appl. Energy 255:113806 (2019), doi:10.1016/j.apenergy.2019.113806.

[9] Ibrahim NI, Al-Sulaiman FA, Rahman S, Yilbas BS, Sahin AZ, "Heat transfer enhancement of phase change materials for thermal energy storage applications: A critical review", Renew. Sustain. Energy Rev. 74:26–50 (2017), doi:10.1016/j.rser.2017.01.169.

[10] Cabeza LF, Fernández AI, Barreneche C, "Introduction to thermal energy storage systems", in: L. F. Cabeza (ed.) *Advances in Thermal Energy Storage Systems (2nd edition)*, Woodhead Publishing (2020). https://doi.org/10.1016/B978-0-12-819885-8.00001-2.

[11] Nižetić S, Jurčević M, Arici M, Valan Arasu A, Xie G, "Nano-enhanced phase change materials and fluids in energy applications: A review", Renew. Sustain. Energy Rev. 129: 109931 (2020), doi:10.1016/j.rser.2020.109931.

[12] Cabeza LF, Zsembinszki G, Martín M, "Evaluation of volume change in phase change materials during their phase transition", J. Energy Storage 28:101206 (2020), doi:10.1016/j.est.2020.101206.

[13] Riahi S, Evans M, Belusko M, Flewell-Smith R, Jacob R, Bruno F, "Transient Thermo-mechanical analysis of a shell and tube latent heat thermal energy storage for CSP plants", Applied Thermal Engineering 196:117327 (2021), doi:10.1016/j.applthermaleng.2021.117327.

[14] Long CS, Loveday PW, "A thermo-hydraulic wax actuation system for high force and large displacement applications", Ind. Commer. Appl. Smart Struct. Technol. 2007. doi:10.1117/12.714737.

[15] Ogden S et al., Review on miniaturized paraffin phase change actuators, valves, and pumps, Microfluid Nanofluid 17:53-71 (2014). https://doi.org/10.1007/s10404-013-1289-3.

[16] Wilhelm E, Richter C, Rapp BE, Phase change materials in microactuators: Basics, applications and perspectives, Sensors and Actuators A 271 (2018). https://doi.org/10.1016/j.sna.2018.01.043.

[17] Ning D et al., Design and Performance Study for Electrothermally Deep-Sea Drive Microunits Using a Paraffin Phase Change Material, Micromachines 12 (2021). https://doi.org/10.3390/mi12040415.

[18] Sulas Industries. Technical Datasheet - HelioDrive Models and Capacities 2020.

[19] U.S. Patent Application, Publication No. US 2012 / 0097149 A1, 2012.

[20] Ramde EW, Tchao ET, Fiagbe YAK, Kponyo JJ, Atuah AS, "Pilot low-cost concentrating solar power systems deployment in sub-saharan Africa: A case study of implementation challenges", Sustainability 12:6223 (2020), doi:10.3390/su12156223.

[21] Leiva-Illanes R, Escobar R, Cardemil JM, Alarcón-Padilla DC, Uche J, Martínez A, "Exergy cost assessment of CSP driven multi-generation schemes: Integrating seawater desalination, refrigeration, and process heat plants", Energy Convers. Manag. 179:249–69 (2019), doi:10.1016/j.enconman.2018.10.050.

[22] N'Tsoukpoe KE, Azoumah KY, Ramde E, Fiagbe AKY, Neveu P, Py X, et al. "Integrated design and construction of a micro-central tower power plant", Energy Sustain. Dev. 31:1–13 (2016), doi:10.1016/j.esd.2015.11.004.

[23] Mendecka B, Lombardi L, "Environmental evaluation of Waste to Energy plant coupled with concentrated solar energy", Energy Procedia, 148:162–169 (2018), doi:10.1016/j.egypro.2018.08.045.

[24] Mendecka B, Lombardi L, Gladysz P, "Waste to energy efficiency improvements: Integration with solar thermal energy". Waste Manag. Res. 37:419–434 (2019), doi:10.1177/0734242X19833159.

[25] Mendecka B, Lombardi L, Gładysz P, Stanek W, "Exergo-ecological assessment of waste to energy plants supported by solar energy", Energies 11:773 (2018). doi:10.3390/en11040773.

[26] Mendecka B, Di Ilio G, Krastev VK, Bella G, "Technical assessment of phase change material thermal expansion for passive solar tracking in residential thermal energy storage applications", J. Energy Storage 48:103990 (2022). doi:10.1016/j.est.2022.103990.

[27] Crescenzi T, Fontanella A, Liberatore R, Russo EM V, "Analisi tecnico-economica di impianti solari a collettori parabolici lineari con differenti fluidi di lavoro" ENEA, Report RdS/2013/077 (2013).

[28] Jo B, Banerjee D, "Thermal properties measurement of binary carbonate salt mixtures for concentrating solar power plants", J. Renew. Sustain. Energy 7:033121 (2015) doi:10.1063/1.4922029.

[29] Araki N, Matsuura M, Makino A, Hirata T, Kato Y, "Measurement of thermophysical properties of molten salts: Mixtures of alkaline carbonate salts" Int. J. Thermophys. 9:1071–80 (1988), doi:10.1007/BF01133274.

[30] Kenisarin MM, "High-temperature phase change materials for thermal energy storage", Renew. Sustain. Energy Rev. 14:955–970 (2010), doi:10.1016/j.rser.2009.11.011.

[31] Tehrani M, Taylor RA, Saberi P, Diarce G, "Design and feasibility of high temperature shell and tube latent heat thermal energy storage system for solar thermal power plants", Renew. Energy 96:120-136 (2016), doi:10.1016/j.renene.2016.04.036.

[32] Cádiz P, Frasquet M, Silva M, Martínez F, Carballo J, "Shadowing and Blocking Effect Optimization for a Variable Geometry Heliostat Field", Energy Procedia 69:60–69 (2015), doi:10.1016/j.egypro.2015.03.008.

[33] Zavoico AB, "Solar Power Tower - Design Basis Document", Tech Rep SAND2001-2100 2001:148. doi:10.2172/786629.

[34] Tehrani M, Shoraka Y, Nithyanandam K, Taylor RA, "Shell-and-tube or packed bed thermal energy storage systems integrated with a concentrated solar power: A techno-economic comparison of sensible and latent heat systems", Appl. Energy 238:887-910 (2019), doi:10.1016/j.apenergy.2019.01.119.

[35] Castell A, Solè C, "An overview on design methodologies for liquid–solid PCM storage systems" Renew. Sustain. Energy Rev 52:289-307 (2015), doi:10.1016/j.rser.2015.07.119

[36] Dutil Y, Rousse DR, Salah NB, Lassue S, Zalewksi L, "A review on phase-change materials: Mathematical modeling and simulations" Renew. Sustain. Energy Rev 15:112-130 (2011), doi:10.1016/j.rser.2010.06.011

[37] Trp A, "An experimental and numerical investigation of heat transfer during technical grade paraffin melting and solidification in a shell-and-tube latent thermal energy storage unit", Sol. Energy, 79:648–60 (2005), doi:10.1016/j.solener.2005.03.006.

[38] Fortunato B, Camporeale SM, Torresi M, Albano M, "Simple Mathematical Model of a Thermal Storage with PCM", AASRI Procedia 2:241–248 (2012), doi:10.1016/j.aasri.2012.09.041.

[39] Esen M, Ayhan T, "Development of a model compatible with solar assisted cylindrical energy storage tank and variation of stored energy with time for different phase change materials", Energy Convers. Manag. 37:1775-1785 (1996).

[40] Visser H, "Energy Storage in Phase-change Materials: Development of a Component Model Compatible with the "TRNSYS" Transient Simulation Program: Final Report", Tech Rep N. EUR-10836-EN, Commission of the European Communities (1986).

[41] Collado FJ, Guallar J, "A review of optimized design layouts for solar power tower plants with campo code", Renew. Sustain. Energy Rev. 20:142–54 (2013), doi:10.1016/j.rser.2012.11.076.

Declaration of interests

☒ The authors declare that they have no known competing financial interests or personal relationships that could have appeared to influence the work reported in this paper.

☐ The authors declare the following financial interests/personal relationships which may be considered as potential competing interests:

Highlights

- Novel concept of passive tracking for concentrated solar power plants
- Numerical modelling of high-temperature latent-heat thermal energy storage
- Exploitation of phase-change induced volumetric expansion for solar tracking
- Passive tracking concept applied to a 15 MWe solar-integrated plant
- Up to 2% of net power output increase achievable thanks to passive tracking